Geometrical Pumping with a Bose-Einstein Condensate

H.-I Lu,[1] M. Schemmer,[1,2] L. M. Aycock,[1,3] D. Genkina,[1] S. Sugawa,[1] and I. B. Spielman[1,*]

[1]*Joint Quantum Institute, National Institute of Standards and Technology,
and University of Maryland, Gaithersburg, Maryland 20899, USA*
[2]*École Normale Supérieure de Lyon, F-69364 Lyon, France*
[3]*Cornell University, Ithaca, New York 14850, USA*

We realized a quantum geometric "charge" pump for a Bose-Einstein condensate (BEC) in the lowest Bloch band of a novel bipartite magnetic lattice. Topological charge pumps in filled bands yield quantized pumping set by the global—topological—properties of the bands. In contrast, our geometric charge pump for a BEC occupying just a single crystal momentum state exhibits nonquantized charge pumping set by local—geometrical—properties of the band structure. Like topological charge pumps, for each pump cycle we observed an overall displacement (here, not quantized) and a temporal modulation of the atomic wave packet's position in each unit cell, i.e., the polarization.

Ultracold atoms in optical lattices provide a unique setting for experimentally studying concepts that lie at the heart of theoretical condensed matter physics, but are out of reach of current condensed matter experiments. Here, we focus on the connection between topology, geometry, and adiabatic charge pumping [1–7] for Bose-Einstein condensates (BECs) in cyclically driven lattice potentials.

Particles in periodic potentials form Bloch bands with energy $\epsilon_n(q)$ and eigenstates $|\Psi_n(q)\rangle = \exp(iq\hat{x})|u_n(q)\rangle$ labeled by the crystal momentum q along with the band index n. The states $|u_n\rangle$ retain the underlying periodicity of the lattice, set by the unit cell size a. Motion in lattices is conventionally understood in terms of these bands: metals are materials with partially filled bands, while insulators have completely filled bands. In this context, a topological charge pump is a counterintuitive device, where charge motion—conduction—accompanies the adiabatic and cyclic drive of an insulating lattice's parameters. Thouless showed that this conduction is quantized, completely governed by the band topology [8,9]. Although various charge pumps have been realized in condensed matter devices—such as modulated quantum dots [10–12], one-dimensional (1D) channels driven by surface acoustic waves [13], and superconducting qubits [14]—Thouless pumps remain unrealized in condensed matter settings but have been demonstrated in recent experiments with cold-atom insulators [15,16].

Here, we break from this established paradigm for insulators and create a quantum charge pump for a BEC in a 1D lattice [17–19] occupying a single crystal momentum state q. This charge pump gives nonquantized motion sensitive to the Berry curvature at q integrated over the whole pump cycle, a local geometric quantity, rather than a global topological quantity. Berry curvatures play an important role in condensed matter systems. An iconic

example is the integer quantum Hall effect, where the electrons acquire an anomalous transverse velocity proportional to the Berry curvature and the quantized Hall conductance is given by the Berry curvature integrated over the whole two-dimensional (2D) Brillouin zone (BZ) [20]; recent cold-atom experiments in 2D have measured such curvatures integrated over part [21,22] or all [23] of the BZ. In an analogous way, 1D lattice systems, driven cyclically in time t, have a generalized Berry curvature defined on the 2D effective BZ in q, t space. This curvature is the source of an anomalous velocity [24], utilized to drive an adiabatic quantum pumping process.

The Rice-Mele model [25–28] of a bipartite lattice with a unit cell consisting of A and B sites is the paradigmatic system for understanding quantum pumps. The Hamiltonian for this tight-binding model is

$$\hat{H}_{RM} = -\sum_j [(t+\delta t)\hat{b}_j^\dagger \hat{a}_j + (t-\delta t)\hat{a}_{j+1}^\dagger \hat{b}_j + \text{H.c.}]$$
$$+ \Delta \sum_j (\hat{a}_j^\dagger \hat{a}_j - \hat{b}_j^\dagger \hat{b}_j), \quad (1)$$

where $\hat{a}_j^\dagger$ and $\hat{b}_j^\dagger$ describe the creation of a particle in unit cell j and sublattice site A or B, respectively. The nominal tunneling strength t is staggered by δt, and the sublattice sites are shifted in energy by Δ.

We investigated quantum pumping in a novel 1D (along $\mathbf{e}_x$) bipartite magnetic lattice (building on Refs. [29,30]) that in effect allowed independent control of t, δt, and Δ. As shown in Figs. 1(a) and 1(b), our magnetic lattice for ^{87}Rb arose from the interplay of one rf and two Raman fields that coupled the $|f=1; m_F = \pm 1, 0\rangle$ "spin" states comprising the $f=1$ ground state hyperfine manifold, which were Zeeman split by $\hbar\omega_Z$. The natural units of momentum and energy are given by the single photon recoil momentum
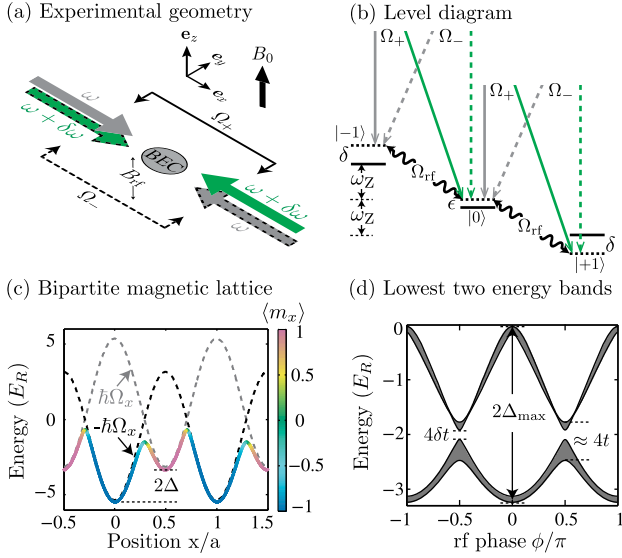
FIG. 1. Bipartite magnetic lattice. [(a) and (b)] Dipole trapped ^{87}Rb BECs subject to a bias magnetic field $B_0 \mathbf{e}_z$ had a Zeeman splitting $\omega_Z/2\pi = 0.817$ MHz and a quadratic shift $\hbar\epsilon = 0.03 E_R$. These BECs were illuminated by four Raman beams and an rf magnetic field. Each of the two Raman couplings (strengths $\Omega_\pm$) was derived from two cross-polarized Raman laser beams with frequency components ω and $\omega + \delta\omega$. (c) Adiabatic potentials colored according to $\langle m_x \rangle$ computed for $\hbar(\bar{\Omega}, \Omega_{\mathrm{rf}}, \delta) = (6, 2.2, 0) E_R$, $\delta\Omega/\bar{\Omega} = -0.1$, and $\phi = \pi/4$. The dashed curves plot the $\pm\hbar\Omega_x$ contributions to the potential experienced by states $|m_x = \pm 1\rangle$. (d) Lowest two energy band energies plotted as a function of ϕ, otherwise with the same parameters as (c).

$\hbar k_R = 2\pi\hbar/\lambda_R$ and its corresponding energy $E_R = \hbar^2 k_R^2/2m$, where m is the atomic mass. In the frame rotating at the rf frequency $\delta\omega$ and under the rotating wave approximation, the combined rf-Raman coupling lead [31] to the overall Hamiltonian

$$\hat{H} = \frac{\hbar^2 \hat{k}_x^2}{2m} + \mathbf{\Omega}(\hat{x}) \cdot \hat{\mathbf{F}} + \hat{H}_Q, \qquad (2)$$

where $\hat{\mathbf{F}}$ is the total angular momentum vector operator. We interpret $\mathbf{\Omega}(\hat{x}) = [\Omega_{\mathrm{rf}}\cos(\phi) + \bar{\Omega}\cos(2k_R\hat{x}), -\Omega_{\mathrm{rf}}\sin(\phi) - \delta\Omega\sin(2k_R\hat{x}), \sqrt{2}\delta]/\sqrt{2}$ as a spatially periodic effective Zeeman magnetic field, in which Ω_{rf} is the rf coupling strength; $\bar{\Omega} = \Omega_+ + \Omega_-$ and $\delta\Omega = \Omega_+ - \Omega_-$ are derived from the individual Raman coupling strengths $\Omega_\pm$; $\delta = \delta\omega - \omega_Z$ is the detuning from Raman-rf resonance; and ϕ is the relative phase between the rf and Raman fields. Additionally, $\hat{H}_Q = -\epsilon(\hbar^2\hat{\mathbb{1}} - \hat{F}_z^2)/\hbar$ describes the quadratic Zeeman shift, where $\hat{\mathbb{1}}$ is the identity operator.

This spatially varying effective magnetic field produces a 1D bipartite lattice [2,32] with lattice constant $a = \lambda_R/2$ and with adiabatic (Born-Oppenheimer) potentials depicted in Fig. 1(c). This magnetic lattice is most easily conceptualized for small $\delta\Omega$: the $\bar{\Omega}\cos(2k_R\hat{x})$ term provides

periodic potentials for the $|m_x = \pm 1\rangle$ states spatially displaced from each other by $a/2$ [dashed curves in Fig. 1(c)]; the resulting $m_x = \pm 1$ sites are then staggered in energy, giving $\Delta \approx \Delta_{\max}\cos(\phi)$, with $\Delta_{\max} = \Omega_{\mathrm{rf}}/\sqrt{2}$. The Ω_y term couples these sublattices together: the rf term $-\Omega_{\mathrm{rf}}\sin(\phi)$ generates constant height barriers (largely specifying t), which become staggered by the $-\delta\Omega\sin(2k_R\hat{x})$ contribution (largely specifying δt).

Figure 1(d) plots the energies of the resulting lowest two bands as a function of ϕ (modulating Δ cosinusoidally). Although our lattice is not in the tight-binding limit, the band structure qualitatively matches that of the Rice-Mele model. In the remainder of this Letter, we focus on the lowest band $n = 0$ and henceforth omit the band index.

As illustrated by the shading in Fig. 1(c), in each unit cell the sublattice sites are labeled by their $\hat{F}_x$ spin projection with the $|m_x = -1\rangle$ site on the left and $|m_x = +1\rangle$ site on the right. To confirm this, we adiabatically loaded $|m_z = -1\rangle$ BECs into the lattice's ground state by simultaneously ramping the detuning from $5E_R$ to 0 while ramping on the coupling fields in 10 ms. Following preparation, our measurement sequence began with a $\pi/2$ spin rotation along $\mathbf{e}_y$, allowing us to measure the eigenstates of $\hat{F}_x$ in our $\hat{F}_z$ measurement basis. We achieved this $\pi/2$ rotation (rot) with a 44 μs pulse from an additional rf field with phase $\phi_{\mathrm{rot}} = \pi/2$ and strength $\hbar\Omega_{\mathrm{rf,rot}} = 2.2 E_R$, applied while the Raman coupling was greatly reduced ($\bar{\Omega} \ll \Omega_{\mathrm{rf,rot}}$) and the lattice rf coupling was off ($\Omega_{\mathrm{rf}} = 0$). We then abruptly removed the remaining control fields along with the confining potential and absorption imaged the resulting spin-resolved momentum distribution after a 20 ms time-of-flight period in the presence of a magnetic field gradient along $\mathbf{e}_y$.

Figure 2 shows the measured $\hat{F}_x$ spin composition [33] and magnetization for adiabatically loaded BECs as a function of ϕ with $\delta\Omega = 0$. Because $\Delta(\phi)$ controls the relative depth of the $|m_x = \pm 1\rangle$ wells, we observe ground state spin populations that follow this "tilt." For example, when $\phi = 0$ or π the double well is strongly tilted and we observe the near perfect spin magnetization, consistent with atoms residing in the individual sublattices; in contrast, when $\phi = \pi/2$, the double wells are balanced and we observe equal populations in each $|m_x\rangle$ state as expected for equal occupancy of both sublattices. Thus, the magnetization [Fig. 2(b)] measures the mean atomic position within each unit cell, i.e., the polarization.

Having constructed a physical realization of the Rice-Mele model, and demonstrated the requisite control and measurement tools, we now turn our attention to topological and geometrical charge pumping. These fundamentally quantum mechanical effects rely on the canonical commutation relation between position and momentum. Consider a finite wave packet with a center of mass (c.m.) position $\langle x \rangle = \langle\Psi|\hat{x}|\Psi\rangle$, subject to a lattice Hamiltonian $\hat{H}$ that is
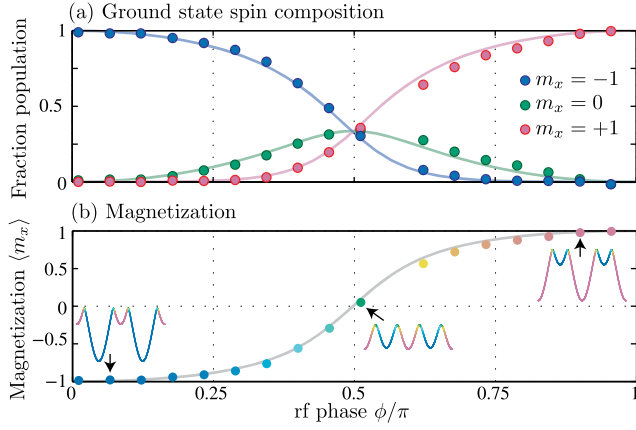
FIG. 2. Ground state spin projections. (a) Ground state spin projections at various ϕ along with the predicted populations for $\hbar(\bar{\Omega}, \delta\Omega, \Omega_{\rm rf}, \delta) = (4.4, 0, 2.2, 0)E_R$. The associated adiabatic potentials [insets in (b)] have minima with spin projection following the observed population's trends. (b) Magnetization derived from data in (a).

adiabatically modulated with period T, i.e., $\hat{H}(t) = \hat{H}(t + T)$. After one cycle, any initial crystal momentum state is transformed, $|\Psi(q)\rangle \to \exp[i\gamma(\hat{q})]|\Psi(q)\rangle$, at most acquiring a phase, where $\hat{q}$ is the crystal momentum operator; this defines the single-period evolution operator $\hat{U}_T = \exp[i\gamma(\hat{q})]$. The time-evolved position operator $\hat{U}_T^{\dagger}\hat{x}\hat{U}_T = \hat{x} - \partial_{\hat{q}}\gamma(\hat{q})$ is displaced after a single pump cycle.

The displacement is particularly simple in two limits: when just a single crystal momentum state is occupied or when every crystal momentum state in the BZ, $-\pi/a \le q < \pi/a$, is occupied with equal probability. As for our BEC, when a single $|q_0\rangle$ state is occupied the displacement is $\Delta x(q_0) = -\partial_q\gamma(q)|_{q_0}$. Both the dynamical (D) phase $\gamma_D(q) = -\bar{\epsilon}(q)T/\hbar$ from the time-average energy $\bar{\epsilon}(q)$ and the geometric Berry (B) phase $\gamma_B(q) = i\int_0^T\langle u|\partial_t u\rangle dt$ contribute to $\gamma(q) = \gamma_D(q) + \gamma_B(q)$. In agreement with conventional descriptions [18,24,27], this predicts a mean velocity $\bar{v}(q) = \partial_q\bar{\epsilon}(q)/\hbar - T^{-1}\int_0^T F(q,t)dt$. The first term is the usual group velocity and the second term—the anomalous velocity—derives from the Berry curvature $F(q,t) = i(\langle\partial_q u|\partial_t u\rangle - \langle\partial_t u|\partial_q u\rangle)$. In our experiment, the BEC occupied the minimum of $\epsilon(q,t)$ at $q = 0$ during the whole pump cycle giving $\partial_q\bar{\epsilon}(q) = 0$, so only the geometric phase $\gamma_B(q)$ contributed to the per-cycle displacement $\Delta x(q = 0) = -\int_0^T F(q = 0, t)dt$.

In the contrasting case of a filled band, the average group velocity is also 0 and the displacement is $\Delta x = -a\int_{\rm BZ}\partial_q\gamma_B(q)dq/2\pi$; this is often expressed as $\Delta x = a\int_0^T\partial_t\gamma_{\rm Zak}(t)dt/2\pi$. The Zak phase $\gamma_{\rm Zak} = i\int_{\rm BZ}\langle u|\partial_q u\rangle dq$, a topological property of 1D bands, is the Berry's phase associated with traversing the 1D BZ once, in the same way that $\gamma_B(q)$ is a Berry's phase taken over a pump cycle.

Our lattice's Zak phase is plotted in Fig. 3(a); this Zak phase is qualitatively indistinguishable from that of the Rice-Mele model, with singularities at $\phi = \pm\pi/2$ and $\delta\Omega = 0$, signaling topological phase transitions across these points. For filled band experiments, pumping trajectories encircling these points give quantized charge pumping [15,16]. Figure 3(b) shows the richly structured Berry curvature $F(q = 0, \phi)$ relevant to our experiment, which is explored next.

For our charge pump experiments, we linearly ramped the pump control parameter $\phi(t) = 2\pi t/T$, effectively modulating the lattice potential in two qualitatively different regimes (separated by a critical $|\delta\Omega/\bar{\Omega}| \approx 0.63$). In the first [Fig. 3(c), left panel] the sublattice sites rise and fall but the local potential minima are essentially fixed in space; in the second [Fig. 3(c), right panel] each minimum is only present for part of the pump cycle (the potential appears to "slide" by $\pm a$ per cycle). As these schematics imply, the associated pumping process gives either no displacement or a quantized per-cycle displacement $\pm a$ for classical trajectories [34]. In quantum systems, however, geometrical
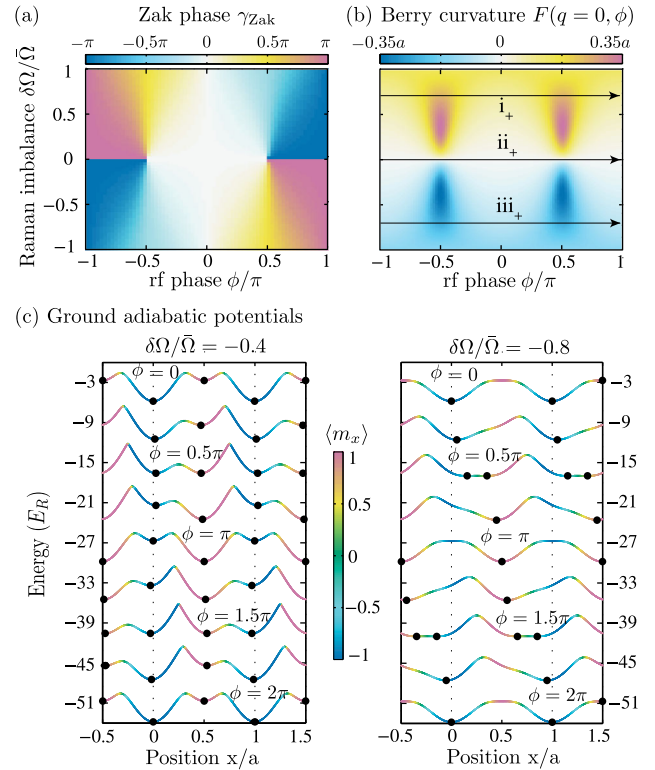
FIG. 3. Band geometry and topology computed for $\hbar(\bar{\Omega}, \Omega_{\rm rf}, \delta) = (6, 2.2, 0)E_R$. [(a) and (b)] Zak phase and $q = 0$ Berry curvature showing the dependence on both $\delta\Omega/\bar{\Omega}$ and ϕ. In (b), the arrows show experimental charge pump trajectories in Fig. 4(b). (c) Adiabatic potentials (displaced vertically for clarity) computed for a range of ϕ constituting a complete pump cycle at $\delta\Omega/\bar{\Omega} = -0.4$ (left panel) and -0.8 (right panel). Filled circles mark the local energy minima.

pumping is controlled by the Berry curvature, giving nonquantized per-cycle displacements that can, in principle, take on any value.

We studied adiabatic charge pumping in this lattice in two ways: in the first we observed the $\hat{F}_x$ magnetization, giving the polarization within the unit cells, and in the second we directly measured the displacement Δx of our BEC. In both cases we loaded into the lattice's ground state and linearly ramped $\phi = 2\pi t/T$, driving the Hamiltonian with period T [34]. As shown in Fig. 4(a), the magnetization oscillated with the $T = 2$ ms period, demonstrating the periodic modulation of polarization per cycle. In good agreement with our data, the solid curves in Fig. 4(a) show the predicted behavior given our known system parameters. This agreement persists to long times: for example, after 50 pumping cycles (for $t = 100$ ms to 110 ms) the contrast is unchanged, confirming the adiabaticity of the process [34].

Lastly, we performed a charge pumping experiment by directly measuring the cloud's position *in situ* for a range of $\delta\Omega/\bar{\Omega}$. We obtained *in situ* density distributions using partial-transfer absorption imaging [35] in which ≈6.8 GHz microwave pulses transferred ≈5% of the atoms from $|f, m_z\rangle = |1, -1\rangle$ to $|2, 0\rangle$ where they were absorption imaged. This technique allowed us to repeatedly measure the *in situ* density distribution for each BEC. Each observed displacement was derived from differential measurements of the cloud position taken just before and just after the pumping process, rendering our observations insensitive to micron-level drift in the trap position between different realizations.

Figure 4(b) shows data taken for $\delta\Omega/\bar{\Omega} = 0.7, 0$, and -0.7 along trajectories i, ii, and iii, respectively, with both increasing and decreasing phases. Our data display two expected symmetry properties. First, since the displacement $\Delta x(q = 0) = -\int F(q, \phi)d\phi$ depends on the sign of the acquired phase, the direction of motion is reversed when the ramp direction is inverted. Second, as shown in Fig. 3(b),

$F(q = 0, \phi)$ is an odd function of $\delta\Omega/\bar{\Omega}$, so the direction of motion is also reversed when $\delta\Omega/\bar{\Omega} \to -\delta\Omega/\bar{\Omega}$. Thus, Δx is an odd function of both ϕ and $\delta\Omega/\bar{\Omega}$, and as expected we observe no motion when $\delta\Omega/\bar{\Omega} = 0$.

The displacement was markedly nonlinear when the pumping time became comparable to our trap's 80 ms period, showing the influence of the confining potential [36]. We included the harmonic potential in our real-space simulations by directly solving the time-dependent Schrödinger equation for our system [37]. The simulated results [Fig. 4(b), solid curves] agree with our observations. To extract the per-cycle displacement due to geometric pumping, we fit the sinusoidal predictions of our model to each data trace, with only the overall amplitudes and a small vertical offset as free parameters, giving the short-time per-cycle displacement [34]. Figure 4(c) shows these per-cycle displacements for a range of Raman imbalances.

The *in situ* cloud typically had a Thomas-Fermi radius of 30 μm, corresponding to a small momentum width of $0.004k_R$ for our BEC. We estimated the thermal fraction to be ≈5% given our ≈20 nK temperature (momentum width of $0.24k_R$). Moreover, the per-cycle displacement is nearly independent of q for $|q| < 0.25k_R$ [34]. These allow us to compare the data with the expected displacement from integrating $q = 0$ Berry curvature [Fig. 4(c), solid line], showing an excellent agreement and confirming the geometric origin of our quantum charge pump.

Our magnetic lattice enables new experiments with 1D topological lattices. Berry curvatures at $q \neq 0$ can be probed by performing the charge pump pairwise at $\pm|q|$ (for example, prepared via Bloch oscillations [38]). The dynamical phases in these cases are opposite and therefore cancel while Berry curvatures (even in q) contribute equally to the displacements [34]. Furthermore, protected edge states, a hallmark of topological systems, are present at the interface between regions characterized by different
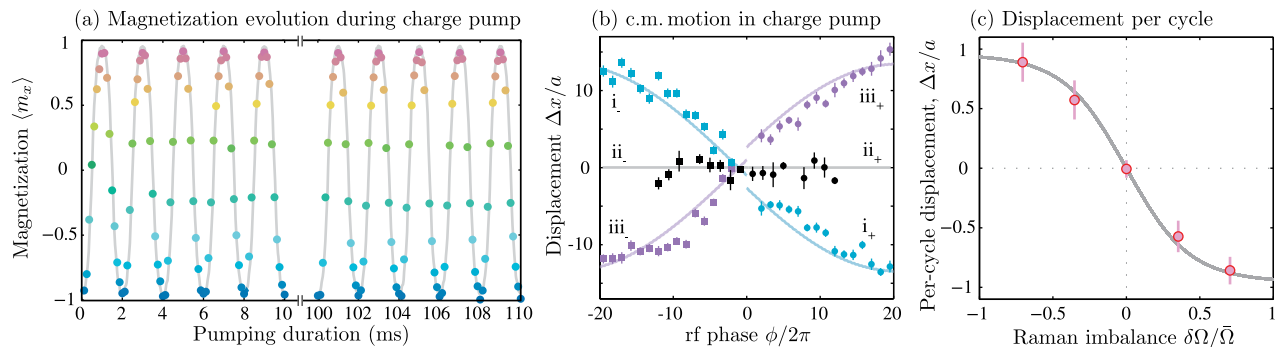
FIG. 4. Geometric charge pumping. (a) Magnetization measured while linearly ramping ϕ with period $T = 2$ ms, along with the prediction for $\hbar\bar{\Omega} = 6.38(2)E_R$, $\hbar\delta\Omega = 4.50(2)E_R$, and $\hbar\Omega_{\rm rf} = 2.20(3)E_R$. (b) Displacement plotted versus $\phi/2\pi$ (number of pump cycles). Trajectories i–iii are taken at $\delta\Omega/\bar{\Omega} = 0.7, 0$, and -0.7, respectively; in each case $\hbar\bar{\Omega} \approx 6E_R$ and $\hbar\Omega_{\rm rf} = 2.20(3)E_R$. Solid curves: simulation of a charge pump in the trap. The small displacement near $\phi = 0$ is introduced by our loading procedure. (c) Measured displacement Δx per pump cycle (symbols), along with the prediction obtained by integrating the Berry curvature over our pumping trajectory (solid curve). The uncertainty bars represent the 95% confidence interval.

topological invariants [39–41]. Since in our lattice the topological index is set by the rf phase, a bulk topological junction can be generated by replacing the rf field with an additional copropagating pair of Raman laser beams in which just one beam has an abrupt π phase shift in its center. This provides a static model of the soliton excitation mode in polyacetylene [25,42]. Terminating our lattice with hard-wall boundaries gives rise to similar end states—somewhat analogous to Majorana fermions in 1D topological superconductors [40,43]—with a spin character.

---

*ian.spielman@nist.gov

[1] F. Mei, J.-B. You, D.-W. Zhang, X. C. Yang, R. Fazio, S.-L. Zhu, and L. C. Kwek, Phys. Rev. A **90**, 063638 (2014).

[2] D.-W. Zhang, F. Mei, Z.-Y. Xue, S.-L. Zhu, and Z. D. Wang, Phys. Rev. A **92**, 013612 (2015).

[3] L. Wang, M. Troyer, and X. Dai, Phys. Rev. Lett. **111**, 026802 (2013).

[4] R. Wei and E. J. Mueller, Phys. Rev. A **92**, 013609 (2015).

[5] T.-S. Zeng, C. Wang, and H. Zhai, Phys. Rev. Lett. **115**, 095302 (2015).

[6] P. Marra, R. Citro, and C. Ortix, Phys. Rev. B **91**, 125411 (2015).

[7] N. R. Cooper and A. M. Rey, Phys. Rev. A **92**, 021401 (2015).

[8] D. J. Thouless, Phys. Rev. B **27**, 6083 (1983).

[9] Q. Niu and D. J. Thouless, J. Phys. A **17**, 2453 (1984).

[10] M. Switkes, C. M. Marcus, K. Campman, and A. C. Gossard, Science **283**, 1905 (1999).

[11] M. D. Blumenthal, B. Kaestner, L. Li, S. Giblin, T. J. B. M. Janssen, M. Pepper, D. Anderson, G. Jones, and D. A. Ritchie, Nat. Phys. **3**, 343 (2007).

[12] B. Kaestner, V. Kashcheyevs, S. Amakawa, M. D. Blumenthal, L. Li, T. J. B. M. Janssen, G. Hein, K. Pierz, T. Weimann, U. Siegner et al., Phys. Rev. B **77**, 153301 (2008).

[13] V. I. Talyanskii, J. M. Shilton, M. Pepper, C. G. Smith, C. J. B. Ford, E. H. Linfield, D. A. Ritchie, and G. A. C. Jones, Phys. Rev. B **56**, 15180 (1997).

[14] M. Möttönen, J. J. Vartiainen, and J. P. Pekola, Phys. Rev. Lett. **100**, 177201 (2008).

[15] S. Nakajima, T. Tomita, S. Taie, T. Ichinose, H. Ozawa, L. Wang, M. Troyer, and Y. Takahashi, Nat. Phys. **12**, 296 (2016).

[16] M. Lohse, C. Schweizer, O. Zilberberg, M. Aidelsburger, and I. Bloch, Nat. Phys. **12**, 350 (2016).

[17] E. Yaschenko, L. Fu, L. Resca, and R. Resta, Phys. Rev. B **58**, 1222 (1998).

[18] R. Resta, J. Phys. Condens. Matter **12**, R107 (2000).

[19] Y. Qian, M. Gong, and C. Zhang, Phys. Rev. A **84**, 013608 (2011).

[20] D. J. Thouless, M. Kohmoto, M. P. Nightingale, and M. den Nijs, Phys. Rev. Lett. **49**, 405 (1982).

[21] G. Jotzu, M. Messer, R. Desbuquois, M. Lebrat, T. Uehlinger, D. Greif, and T. Esslinger, Nature (London) **515**, 237 (2014).

[22] L. Duca, T. Li, M. Reitter, I. Bloch, M. Schleier-Smith, and U. Schneider, Science **347**, 288 (2015).

[23] M. Aidelsburger, M. Lohse, C. Schweizer, M. Atala, J. T. Barreiro, S. Nascimbène, N. R. Cooper, I. Bloch, and N. Goldman, Nat. Phys. **11**, 162 (2015).

[24] S.-Q. Shen, Topological Insulators: Dirac Equation in Condensed Matters (Springer, New York, 2012), Vol. 174.

[25] W. P. Su, J. R. Schrieffer, and A. J. Heeger, Phys. Rev. Lett. **42**, 1698 (1979).

[26] M. J. Rice and E. J. Mele, Phys. Rev. Lett. **49**, 1455 (1982).

[27] D. Xiao, M.-C. Chang, and Q. Niu, Rev. Mod. Phys. **82**, 1959 (2010).

[28] M. Atala, M. Aidelsburger, J. T. Barreiro, D. Abanin, T. Kitagawa, E. Demler, and I. Bloch, Nat. Phys. **9**, 795 (2013).

[29] K. Jiménez-García, L. J. LeBlanc, R. A. Williams, M. C. Beeler, A. R. Perry, and I. B. Spielman, Phys. Rev. Lett. **108**, 225303 (2012).

[30] L. W. Cheuk, A. T. Sommer, Z. Hadzibabic, T. Yefsah, W. S. Bakr, and M. W. Zwierlein, Phys. Rev. Lett. **109**, 095302 (2012).

[31] G. Juzeliūnas and I. B. Spielman, New J. Phys. **14**, 123022 (2012).

[32] N. Lundblad, S. Ansari, Y. Guo, and E. Moan, Phys. Rev. A **90**, 053612 (2014).

[33] The data presented in Fig. 2 contain a small correction from the known imperfect state rotation.

[34] See Supplemental Material at http://link.aps.org/supplemental/10.1103/PhysRevLett.116.200402 for simulations of classical pumps, Berry curvatures and geometric pumps at nonzero, and other experimental details.

[35] A. Ramanathan, S. R. Muniz, K. C. Wright, R. P. Anderson, W. D. Phillips, K. Helmerson, and G. K. Campbell, Rev. Sci. Instrum. **83**, 083119 (2012).

[36] The effective mass in the lattice can increase the period.

[37] W. Bao, D. Jaksch, and P. A. Markowich, J. Comput. Phys. **187**, 318 (2003).

[38] M. B. Dahan, E. Peik, J. Reichel, Y. Castin, and C. Salomon, Phys. Rev. Lett. **76**, 4508 (1996).

[39] J. Ruostekoski, J. Javanainen, and G. V. Dunne, Phys. Rev. A **77**, 013603 (2008).

[40] M. Z. Hasan and C. L. Kane, Rev. Mod. Phys. **82**, 3045 (2010).

[41] S. Ganeshan, K. Sun, and S. D. Sarma, Phys. Rev. Lett. **110**, 180403 (2013).

[42] A. J. Heeger, S. Kivelson, J. R. Schrieffer, and W. P. Su, Rev. Mod. Phys. **60**, 781 (1988).

[43] S. Nadj-Perge, I. K. Drozdov, J. Li, H. Chen, S. Jeon, J. Seo, A. H. MacDonald, B. A. Bernevig, and A. Yazdani, Science **346**, 602 (2014).